RSC Applied Interfaces

ROYAL SOCIETY OF CHEMISTRY

PAPER

View Article Online
View Journal

Check for updates

Cite this: DOI: 10.1039/d5lf00341e

Phototunable hopping of microparticles enables surface-selective continuous separation *via* microfluidics

Fabian Rohne, [a] Daniela Vasquez Muñoz,[a] Yulia Gordievskaya,[a] Cevin Braksch,[a] Isabel Meier,[a] Anjali Sharma,[a] Sarah Loebner,[a] Anne Nitschke,[b] Nino Lomadze,[a] Andreas Taubert,[b] Svetlana Santer [a] and Marek Bekir *[a]

Received 4th November 2025,
Accepted 16th March 2026

DOI: 10.1039/d5lf00341e

rsc.li/RSCApplInter

High surface area materials are central to next-generation technologies, yet their purification remains limited by lab-scale methods. We present a continuous-flow technique that separates microparticles by surface area and porosity. The method relies on light-responsive surfactants that generate surface-localized photochemical activity under illumination, scaling with particle surface area. Particles with sufficient activity undergo light-induced "hopping" into an overlying channel, enabling deflection across streamlines and obstacles. Non-porous particles remain confined, while porous particles are diverted to secondary outlets. We demonstrate control of hopping efficiency through illumination parameters, establishing a scalable platform for high-throughput, surface-sensitive purification.

Open Access Article. Published on 02 April 2026. Downloaded on 4/25/2026 12:59:56 PM.
This article is licensed under a Creative Commons Attribution 3.0 Unported Licence.

Introduction

Next-generation applications increasingly demand advanced functional materials with highly specialized properties. Among the wide array of critical material characteristics, one universally advantageous and frequently required attribute, particularly for dynamic and responsive systems, is a high specific surface area. Materials exhibiting high surface areas offer enhanced interfacial contact with their environment, thereby significantly improving mass and energy exchange processes and enabling a more efficient response to external stimuli.

This makes porous microparticles of growing considerable interest, as their high surface-to-volume ratios underpin performance enhancements across a diverse range of technological applications.[1] These include heterogeneous catalysis,[2–4] next-generation battery systems,[5–7] fabrication of porous 2d macroscopic interfaces with colloidal lithography,[8] heat-energy storage media,[9] and adsorption-based technologies such as activated carbon for wastewater treatment,[10–12] among others.[13–16] In each of these fields, the porous architecture of the particles directly influences functional efficiency, making morphological control, especially porosity, a central design criterion.

However, the scalable fabrication of such porous microparticles remains a significant challenge. Conventional synthesis methods often yield particles with broad distributions in size and structural heterogeneity, particularly in terms of porosity and internal surface area. Such variability can severely compromise performance consistency in end-use applications. For instance, in catalysis or electrochemical energy storage, minor deviations in surface area can lead to disproportionately large drops in activity or capacity.

Therefore, beyond size-based classification, it is important to develop strategies for the selective separation and fractionation of particles based on their porosity or, effectively, their accessible surface area. Despite the widespread use of particle sizing techniques at both laboratory[17–21] and industrial scales,[22–24] methods for surface based (includes porosity based) separation have only recently gained traction, driven largely by advances in surface-chemistry-mediated fractionation approaches.[25] Recent advances have demonstrated the integration of phoretic or osmotic activity with microfluidic platforms, wherein colloidal particles are suspended in aqueous media containing dissolved salts.[25] By employing controlled injection protocols to establish localized salt concentration gradients, active colloids can be guided toward specific regions within the microchannel. Under laminar flow conditions, this method facilitates selective migration, segregation, and subsequent collection of particles through spatially separated outlets under continuous operation. Rather than relying on microfluidic-based fractionation techniques, Zheng *et al.* demonstrated that particles can be locally separated and remotely guided to predefined location

[a] *Institute of Physics and Astronomy, University of Potsdam, 14476 Potsdam, Germany. E-mail: marek.bekir@uni-potsdam.de*
[b] *Institute of Chemistry, University of Potsdam, 14476 Potsdam, Germany*

Open Access Article. Published on 02 April 2026. Downloaded on 4/25/2026 12:59:56 PM.
This article is licensed under a Creative Commons Attribution 3.0 Unported Licence.

down to micron scale through spatially controlled light illumination. This approach is enabled by functionalizing the particles with light-responsive dyes, allowing selective manipulation *via* externally applied illumination patterns.[26] An alternative approach for particle separation leverages differences in interfacial properties by exploiting surface morphology characteristics such as roughness, porosity, and surface charge. This strategy offers enhanced flexibility, enabling the discrimination of particles with identical sizes but distinct surface chemistries or interfacial compositions.[27,28]

Surface-sensitive fractionation can be realized through the integration of microfluidic technology with light-induced phoretic activity of microparticles, as illustrated in Scheme 1. Initially, microparticles are suspended in a solution containing a photo-responsive surfactant, {(6-[4-(4-hexylphenylazo)-phenoxyl-butyl-trimethylammoniumbromide], abbreviated $AzoC_6$, (Scheme 1))},[27] and subsequently introduced into the microfluidic channel. Sedimented microparticles move along with the carrier fluid flow inside the separation cell. Upon illumination, the photo-responsive surfactant renders the particles to be phoretic/osmotic active due to the release of *cis* isomers from particles interface.[27,28] The bottom wall acts as a reflective boundary for the *cis*-isomers, which cause a hovering of the sedimented particles during light illumination. It has been previously demonstrated that hovering height and translational velocity of the particles depends on the strength of the light induced activity and thus on the interfacial properties of the particles themselves.[27,28]

Two principal illumination strategies may be employed: global[27,28] and locally[29] collimated light profiles. In the case of global collimation, as illustrated in Scheme 1, the entire separation region is uniformly illuminated. This results in a sustained velocity difference between distinct particle fractions, enabling separation based on retention principles.[30,31] The method benefits from low-cost instrumentation and straightforward sample preparation; however, its primary limitation lies in throughput.[28,32] Since the separation process operates in a batchwise manner, it is less suited for high-throughput applications involving large quantities of dispersed particles.

To improve the throughput, one needs to transition from a batchwise to a continuous separation mode. This forms the central focus of the present study, in which we propose a framework for continuous, surface-sensitive separation based on locally collimated light illumination, as depicted in Scheme 1. In this approach, particles entering the illuminated region experience a transient enhancement in phoretic activity, which can be sufficiently strong to enable them to traverse physical obstacles. Specifically, this activity allows certain particles to be levitated into a secondary, elevated microchannel, from which they are extracted *via* a separate outlet. Such selective fractionation based on interfacial properties is feasible only for particles exhibiting sufficiently strong light-induced phoretic responses.[27] For example, only particles with high surface porosity may generate enough propulsion to surmount step heights of approximately 100 μm along otherwise planar interfaces. Such high levitation requires strong phoretic activity, which can be achieved by using the principles of *l*-LDDO only when the applied wavelength is in the UV range.[33,35,36]

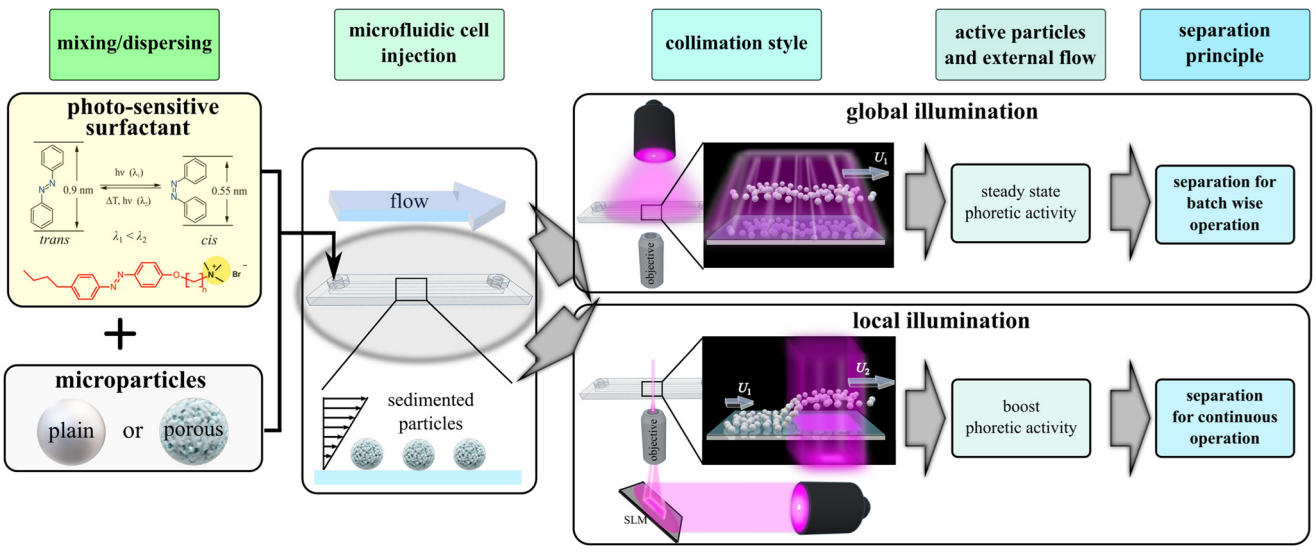

Scheme 1 Schematic overview of surface sensitive separation principles. Microparticles are dispersed in aqueous solution containing $AzoC_6$ (c_{azo} = 1 mM). After equilibration time (~1 day) the dispersion is injected into separation cell (microfluidic chamber composed of glass transparent in UV range). Particles sediment at the substrate bottom in the separation cell. Separation principle under global (top) or local light (bottom) illumination. Global illumination causes particles to hover continuously, but only over short distances, leading to velocity differences and separation by elution, similar to gravitational field-flow fractionation. This process is simple but limited to batch operation. In contrast, localized illumination (in particular UV light, λ = 365 nm) induces transient hovering, lifting particles several micrometers into the channel void, where they can enter a second, higher channel position. Under locally collimated light, particles can permanently hop over obstacles, enabling a continuous separation process.

© 2026 The Author(s). Published by the Royal Society of Chemistry

Open Access Article. Published on 02 April 2026. Downloaded on 4/25/2026 12:59:56 PM.
This article is licensed under a Creative Commons Attribution 3.0 Unported Licence.

We previously demonstrated particle fractionation in batchwise operation using a modified field-flow fractionation (FFF) principle.[36] This approach was shown to be effective for several distinct particle pair types, including particles with porous *versus* non-porous interfacial structures,[27] particles composed of different polymeric materials by tuning the wavelength of the applied illumination,[28] and particles exhibiting only minor differences in surface functionalization through the use of a chemically active interface.[31]

The approach presented in this work departs from these earlier studies[27,28,31,36] by translating the separation concept from batchwise to continuous operation. While the same aqueous photosensitive surfactant solution is employed, the separation mechanism is fundamentally changed by replacing global illumination with spatially localized light collimation. This modification enables particle levitation above obstacles and enables continuous selective fractionation of one species. In the following, we first analyze the levitation strength as a function of illumination wavelength, followed by a demonstration of how this effect can be employed as a continuous separation mechanism.

Theory: from velocity as a proxy to predict levitation height as a function of the wavelength

The levitation dynamics of particles suspended in fluid within a laminar microchannel are strongly governed by the local hydrodynamic environment. Owing to their comparatively large mass and micron-scale dimensions, yet still being much smaller than the characteristic geometric length scale of the channel (height = 0.54 mm), the particles undergo gravitational sedimentation. Consequently, they remain confined to a narrow near-wall region, either in direct contact with the bottom surface or levitated only a few micrometers above it. In this regime, the local flow field can be approximated by a linear shear profile, consistent with low-Reynolds-number hydrodynamics under Stokes flow conditions. When a particle is levitated at a height h_{ac} above the lower wall (see for illustration Fig. S1), it is situated in a region of laminar flow with a spatially varying velocity gradient. In this regime, conservation of mass and momentum leads to the development of a net drift velocity U, which scales with the local shear rate S. This shear rate is evaluated at a vertical position equal to the sum of the particle radius and levitation height, $h_{ac} = a + h_{lev}$, where the flow profile remains approximately linear. Consequently, the particle's translational motion is governed by its hydrodynamic interaction with the spatially varying flow field at that elevation. Under the assumption that particles are positioned at the mid-width of a rectangular microchannel (Scheme 1) Brenner *et al.* derived an asymptotic expression,[37,38] where the hovering tendency is connected with translational velocity as:[27,28,36,37,39]

$$U = S \cdot h_{ac} \cdot \left(1 - \frac{5}{16} \cdot \left(\frac{a}{h_{ac}}\right)^3\right) \quad (1)$$

where S is the applied shear rate, a the particle radius and h_{ac} the hovering height of the particle. If the hovering is much larger than the particle radius $h_{ac} \gg a$ the asymptotic expression $\frac{5}{16} \cdot \left(\frac{a}{h_{ac}}\right)^3$ is very small and can be omitted in first approximation. This assumption holds true for strongly hovered particles discussed later in the results and discussion section under local light collimation. Then eqn (1) simplify into:

$$U \sim S \cdot h_{ac} = S \cdot (a + h_{lev}), \quad (2)$$

where per definition (see Fig. S1) h_{ac} is the sum of particle radius plus the minimum separation distance between the bottom particle surface and the channel substrate, thus $h_{ac} = a + h_{lev}$. From eqn (2) we calculate the value of levitation height:

$$h_{lev} \sim \frac{U}{S} - a. \quad (3)$$

Results and discussion

Systematic investigation of velocity boost as a function of the wavelength

Before introducing the concept of continuous separation, we first address the rationale for employing UV light illumination. This choice is motivated by a systematic investigation of particle hovering behavior as a function of illumination wavelength. In all experiments, two illumination strategies were implemented: local and global collimation. The corresponding illuminated regions are shown for UV light in Video S1 and as snapshot series in Fig. 1a–d. Particle motion was quantified by tracking individual trajectories across the illumination region. For each frame, the mean particle velocity was calculated from all crossing trajectories, and the temporal evolution of the average velocity (bold line) together with the standard deviation (shaded region) is reported for local (Fig. 1b and d) and global collimation (Fig. 1a and c). All experiments were conducted in a rectangular microfluidic channel (height h = 0.54 mm, width w = 3.8 mm, length L = 17 mm) at a constant volumetric flow rate of 150 μL min^{-1}, corresponding to a shear rate of 14.98 s^{-1} as determined from eqn (13) (Materials and methods section).

Under local light collimation and particularly for UV light data exhibit a constant strong boost of entering microparticles and thus the average velocity maintains for the whole-time frame of illumination, while at global light particles experience a transient boost with subsequent decay to the initial velocity at no illumination. It is important to note that collimation from the bottom

Open Access Article. Published on 02 April 2026. Downloaded on 4/25/2026 12:59:56 PM.
This article is licensed under a Creative Commons Attribution 3.0 Unported Licence.

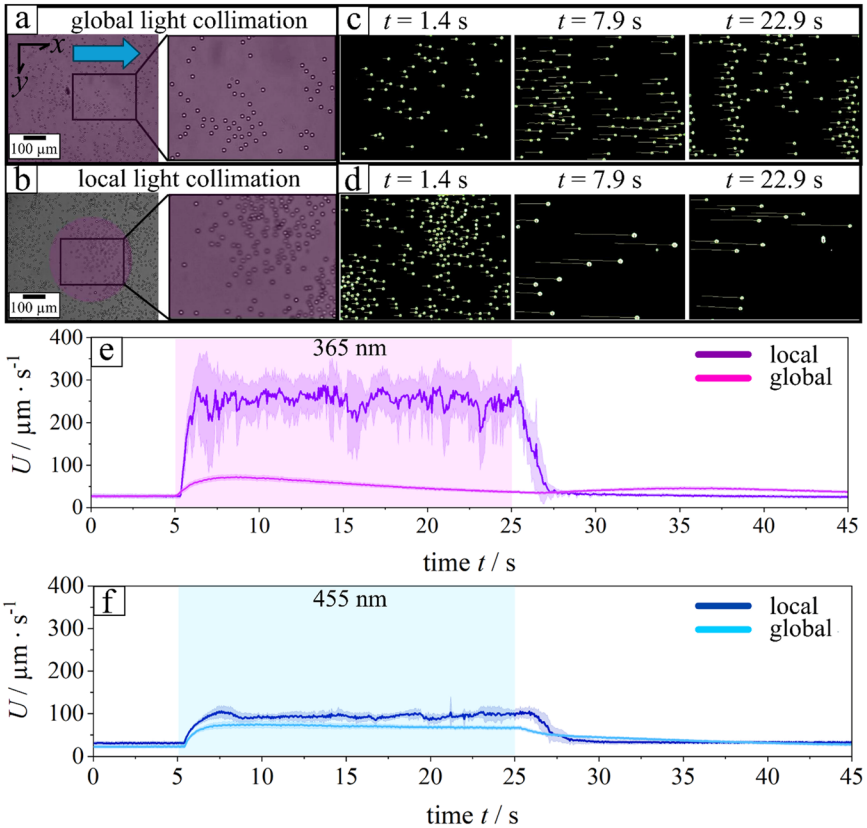

Fig. 1 (a and b) Snapshots illustrating the two illumination strategies: (a) globally and (b) locally collimated UV light (λ = 365 nm) at identical applied power (P = 11.45 mW). Data are taken from Video S1. (b and d) Processed images with particle trajectories over a 1 s recording window, shown before illumination (1.7 s), during illumination (7.9 s), and after switching off the light (22.9 s). (c) Corresponds to global illumination, (d) to local illumination. (e) Time-resolved average velocity obtained from trajectory analysis for Video S1 (365 nm) and (f) for Video S2 (455 nm).

substrate minimizes the optical path length through the microfluidic channel. This improves the boosting tendency of chemical activity of the microparticles and strongly impact the levitation height (Fig. 2).

The average steady-state velocity, plotted in Fig. 3c and d for the final 5 s of illumination (t = 20–25 s), reveals that light-induced motion varies not only in velocity profile as a function of wavelength but also in absolute magnitude. Velocities under local illumination (see Fig. 3c) are consistently higher compared to global collimation (see Fig. 3d). Although the applied power was kept constant in all experiments (P = 11.5 mW), local collimation through the objective confines the light to a rectangular spot of only a few micrometers (200 × 300 µm), additionally loses power output leaving the objective to 0.8 mW, thereby substantially increasing the local intensity. This enhanced intensity amplifies the phoretic/osmotic activity, which scales with light intensity. As a result, particles exhibit stronger activity, attain larger hovering heights (h_{ac}), and reach higher velocities in agreement with eqn (1). In the following, we discuss in more detail the differences in motion patterns between the two collimation strategies.

Global light illumination. For global light illumination, a detailed explanation has already been provided in ref. 28 and the corresponding SI. In brief, the phoretic/osmotic activity arises from the formation of a *cis*-isomer gradient and is therefore governed by the photoisomerization kinetics at the microparticle interface. A highly simplified description that considers only the *cis*-isomer conversion rate at the interface cannot capture all details (for a comprehensive discussion, see ref. 28), but it conveys the essential trend: the particle velocity varies systematically with illumination wavelength:

$$\text{constant flux} \sim \frac{dc_p}{dt} = k_{TC,I}(\lambda)\cdot I\cdot A_{eff}\cdot\theta_T \quad (4)$$

with I as applied light intensity, $k_{TC,I}$ the photoisomerization rate constant at given wavelength, A_{eff} the effective surface area of the particles and θ_T as the *trans* isomer surface coverage. Two key parameters are of significant importance, the value of $k_{TC,I}$ and θ_T. Now, the increase of applied wavelength yields in a decrease in the value of $k_{TC,I}$ and increase of the value of the *trans*-isomer surface coverage, θ_T. The latter results from an increase of the *trans* isomer fraction with increasing wavelength.[28] This cause the *cis* isomer conversion rate (~*cis* isomer flux), basically the product of both, to peak at a maximum for 405/415 nm of radiation wavelength and so follows the translation velocity due to hovering, too (Fig. 3d).[28]

Local light collimation. For local light collimation the general assumption of phoretic activity connected by the relation eqn (4) holds true as well but with only one

© 2026 The Author(s). Published by the Royal Society of Chemistry

Open Access Article. Published on 02 April 2026. Downloaded on 4/25/2026 12:59:56 PM.
This article is licensed under a Creative Commons Attribution 3.0 Unported Licence.

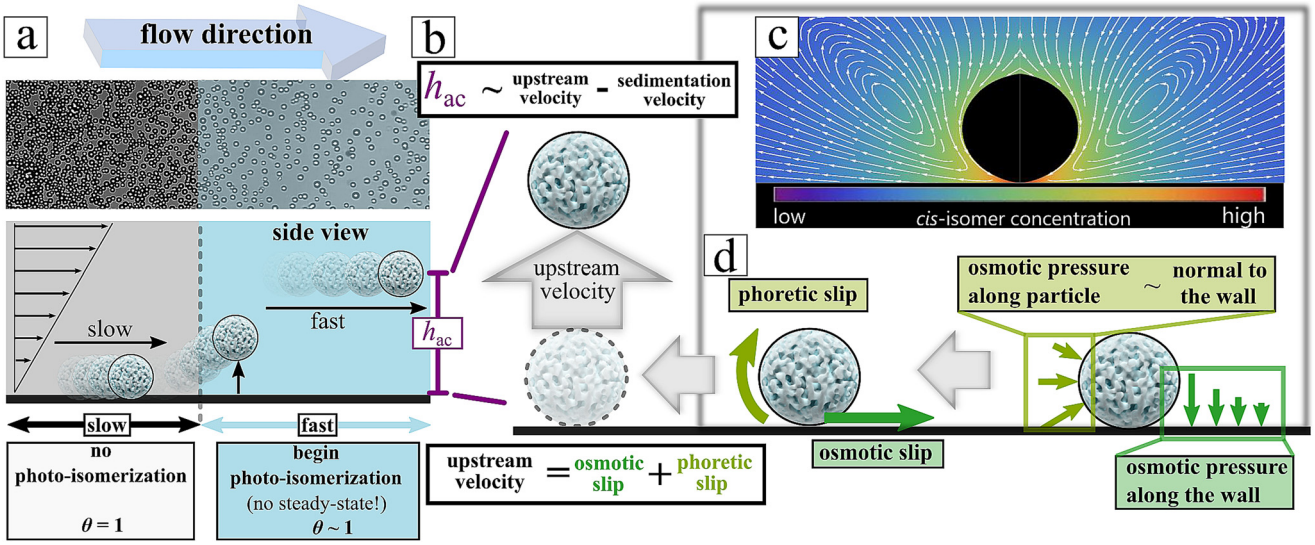

Fig. 2 (a) Optical micrograph (top) and schematic side view (bottom) of porous microparticles entering the illuminated area, where surface coverage of *trans*-isomers is maximal (θ = 1). Dynamic exchange has not yet reached steady state, so the interface remains fully covered. Blue arrow: flow direction. (b) Phoretic activity lifts the particles to an equilibrium height h_{ac}, defined by the balance of light-induced upstream and sedimentation velocities. Osmotic (dark green) and phoretic (olive green) contributions are indicated. (c) Local *cis*-isomer concentration gradients form around the particles (purple = low c_{cis}, red = high c_{cis}; white arrows: fluid flow). (d) Vertical and horizontal osmotic pressure gradients (olive, dark green) decay into the bulk and control the light-induced upstream velocity.

difference that the surface coverage of *trans* isomers, θ_T is always 1 instead in global light collimation to be fraction between 0 and 1. Then eqn (4) simplifies into:

$$\text{constant flux} \sim \frac{dc_p}{dt} = k_{TC,I}(\lambda)\cdot I\cdot A_{eff} \quad (5)$$

Upon entering the illuminated region (Video S3, snapshot (Fig. 2a)), particles experience photoisomerization in both bulk solution and at their interface, leading to complete *trans*-isomer coverage. Over the crossing time (~4 s), this coverage remains effectively unchanged, as the induced velocities prevent significant depletion. We therefore assume θ_T = 1 for all particles within the illuminated area. Under this condition, the velocity exhibits a linear dependence on the photoisomerization rate constant $k_{TC,I}$ = k_{TC} and the effective particle area A_{eff}, consistent with experimental observations (Fig. 3).

Data exhibit that the velocity follows the pattern of the *trans* isomer absorption spectrum. We explain this relation by the fact that the value of the photoisomerization rate constant is the product of the quantum yield φ, the extinction coefficient ε and the applied intensity of illumination I:[40]

$$k_{photoisomerization} = \varphi\cdot\varepsilon\cdot I. \quad (6)$$

And since the intensity already has been extracted here out[33] and kept fixed, the magnitude of the velocity and hovering height is proportional to ε_T (λ) for each wavelength, due to ~$U(\lambda)$ ~$h_{ac}(\lambda)$ ~$k_{TC}(\lambda)$ ~ε_T (λ). This means that under local illumination one can approximate the light induced levitation strength (Fig. 4b and c) and translational velocity boost of particles (Fig. S3b and c) from the absorbance spectrum of the photo switch. Apparently, the *trans* isomer has a peak maximum at 351 nm and so the velocity boost is the strongest in UV range with increasing value towards blue shift. This means the strongest levitation of microparticles can be expected under illumination in UV range (Fig. 4b and c).

Hovering of particles over obstacles for continuous separation. Strong levitation allows microparticles to cross obstacles taller than their diameter, provided they exhibit sufficient phoretic activity. We demonstrate this by hovering 5 μm porous particles over a 100 μm wall (two tape layers; Video S4, Fig. 5c and e). The wall is angled ~40° to deflect passive momentum and reduce accumulation. UV illumination enables on-demand "hop on/hop off" motion over the wall, allowing remote guidance of particles along different streamlines.

Apparently, we observe that the levitation of the particle can be lower than the height of the obstacle as data in Fig. 5e and Video S4 clearly demonstrate a wall lift migration, while calculated levitation height h_{lev} is much lower. We estimated the needed minimum elevation height of particles by calculating the value of h_{lev} using eqn (3) in absence of any obstacle, where the applied illumination intensity has been precisely varied displayed in Fig. S5a. Then we compared the value of h_{lev} with the hopping potential over the obstacle by performing same measurements with same variation in intensity displayed in Fig. S5b. Data exhibits that already 5 μm of levitation, approximately one diameter, is enough to successfully hop particles over the obstacle. Thus, besides the light induced levitation, hydrodynamic effects appear to play a critical role in the system, particularly in regions proximal to obstacles,

Open Access Article. Published on 02 April 2026. Downloaded on 4/25/2026 12:59:56 PM.
This article is licensed under a Creative Commons Attribution 3.0 Unported Licence.

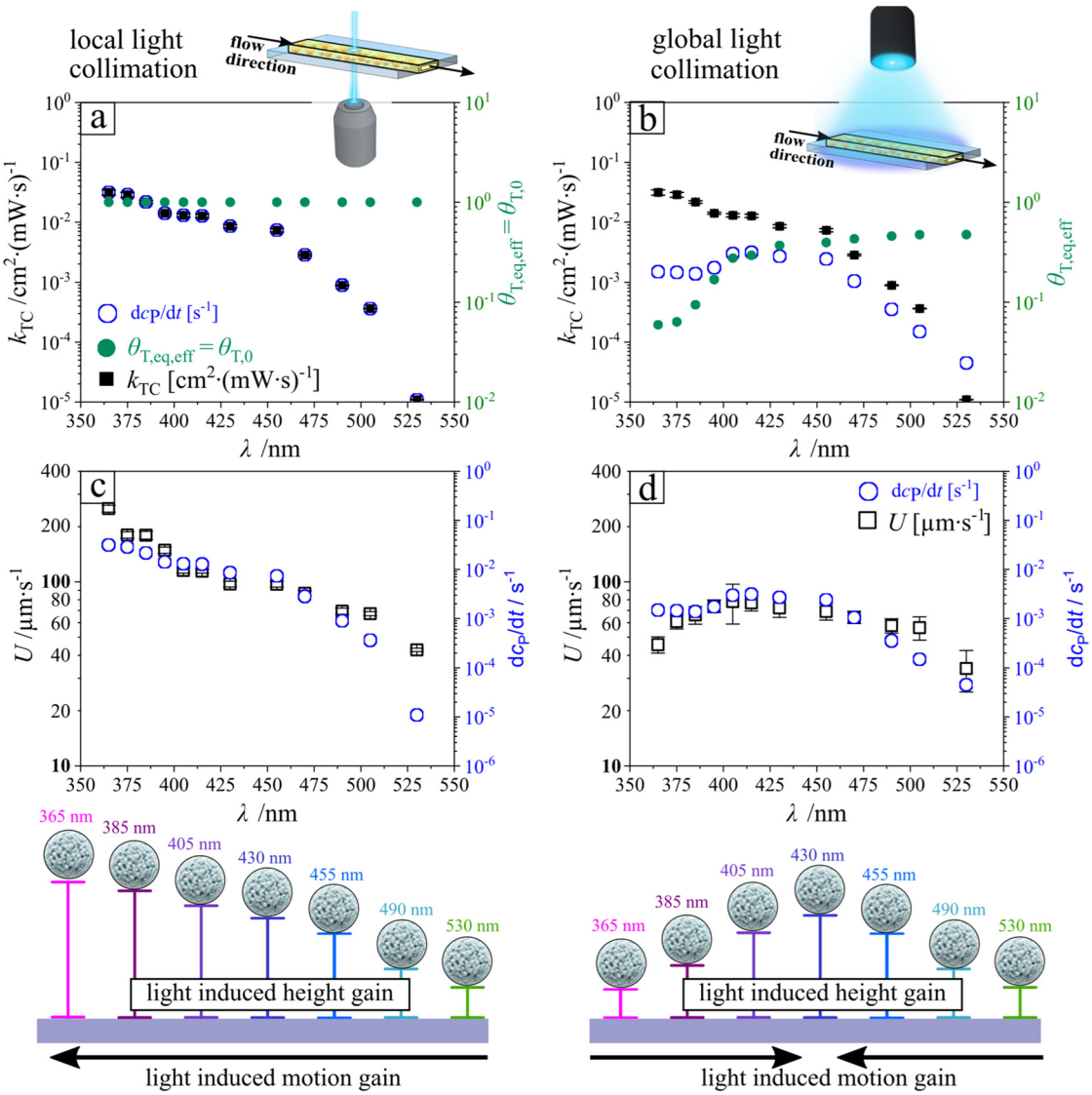

Fig. 3 Key photochemical parameters under local (left, a and c) and global (right, b and d) illumination. (a and b) Steady-state isomer flux, dc_P/dt, *trans*-isomer coverage θ_T, and *trans*-to-*cis* rate constant k_{TC} as a function of wavelength, indicating local photoactivity and effective *l*-LDDO strength. (c and d) Corresponding particle velocities under the same spectral conditions, differing only in illumination geometry. Data in (b and d) are reproduced from ref. 28 to highlight the impact of illumination collimation on particle dynamics. Note, that local light collimation from the bottom of the substrate minimizes the optical pathway and drastically improves the boosting in levitation.

where particle lift forces are significantly amplified. In general, when particles are in close proximity to channel walls or the bottom substrate, they experience a transverse pressure gradient. This gradient induces a hydrodynamic lift force directed away from the lower boundary (substrate) toward the center of the channel. This near-wall lift force F_{Nw} given by:[41–43]

$$F_{Nw} = \frac{6 \cdot C \cdot \eta \cdot a^3}{h_{lev}} \cdot S \tag{7}$$

where, C is the empirical, dimensionless coefficient; η the dynamic viscosity of the carrier fluid; S the local shear rate of the fluid near the channel bottom substrate; a the radius of the suspended particle; and h_{lev} the minimum separation distance between the particle surface and the channel wall. As the particle moves away from the substrate, the hydrodynamic lift force increases until it counterbalances the gravitational force at a specific equilibrium position. In regimes where inertial contributions to the lift force are negligible (*i.e.*, low Reynolds number or Stokes flow conditions), the net force is given by:

$$F_{net} = F_{Nw} - F_G = \frac{6 \cdot C \cdot \eta \cdot a^3}{h_{lev}} \cdot S - \frac{4}{3} \cdot a^3 \cdot \Delta\rho \cdot G, \tag{8}$$

where F_G is the gravitational force acting on the particle, with a density difference $\Delta\rho$ relative to the carrier fluid, G the gravitational acceleration, typically taken as 9.81 m s^{-2}. At equilibrium position the force F_{net} = 0 and eqn (8) can be rewritten into:[44]

© 2026 The Author(s). Published by the Royal Society of Chemistry

Open Access Article. Published on 02 April 2026. Downloaded on 4/25/2026 12:59:56 PM.
This article is licensed under a Creative Commons Attribution 3.0 Unported Licence.

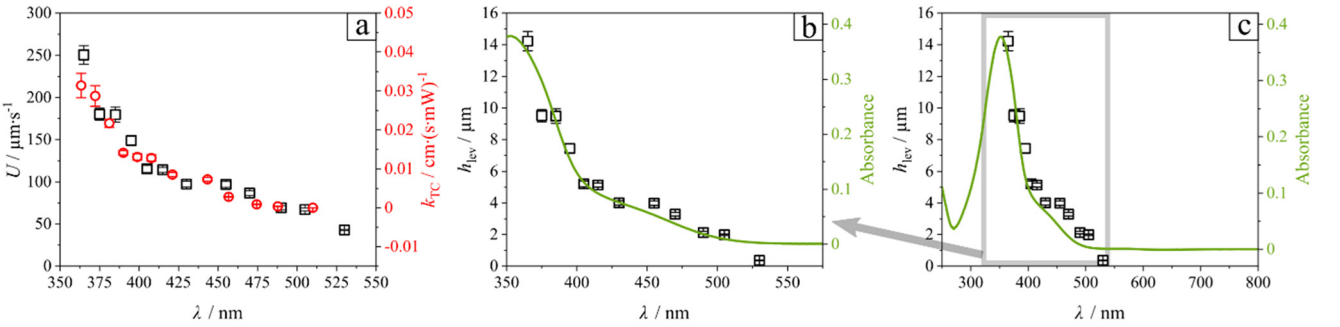

Fig. 4 (a) Particle velocity under spectrally resolved illumination (dark hollow rectangles) overlaid with the *trans*-to-*cis* isomerization rate constant k_{TC} (red hollow circles), showing the spectral dependence of drift motion. (b and c) Measured hovering height (dark hollow rectangles) is compared with the UV-vis absorbance of the *trans*-isomer (c = 0.1 mM), highlighting the correlation between spectral absorption and light-induced motion. A corresponding velocity plot is provided in Fig. S3 (SI).

$$h_{lev} = \frac{9}{2}\cdot\frac{C\cdot\eta}{\Delta}\rho\cdot G\cdot S. \quad (9)$$

In other words, particles according to density migrate under shear already to a certain elevation zone depending on the fluid velocity (~shear rate S) but are independent of the particle size. This is irrespective of the light induced levitation. Now when particles come close to the obstacle the local laminar flow field may yield to additional perturbation and influences shear-induced rotation of the particle, *i.e.* increases near-wall lift force F_{Nw}. Note, neither eqn (1)–(3) nor (9) are valid for flow fields close to the proximity to obstacles. This means a stronger lift force might appear, where light induced hovering is additionally manipulated.

Thus, to further support the demonstration of the separation potential of hopping particles traversing diagonal obstacles, we perform numerical simulations of the fluid flow field using the COMSOL Multiphysics software. The simulation domain is illustrated in Fig. 5f, and representative cross-sectional velocity field profiles are presented in Fig. 5g both in the plane normal to the flow (top) and along the flow direction (bottom). As shown in Fig. 5g, the computed flow streamlines indicate that fluid can only traverse around the obstacle at specific vertical (z) positions within the microchannel. And if the light induced hovering reaches the critical vertical position the remaining distance can be overcome from the carrier fluid.

Notably, at an elevation corresponding to the particle radius (z = 2.5 μm), streamlines are directed from the vicinity of the wall toward outlet channel (bottom) (Fig. 5h, left). This result aligns with experimental observations from Video S4, where microparticles are passively advected along the wall when the illumination is off. At higher vertical positions specifically at the top of the obstacle (z = 102.5 μm, Fig. 6h, middle) and significantly above it (z = 202.5 μm, Fig. 5h, right) the flow streamlines are directed toward the upper outlet channel (top), with some extend in lateral deflection toward outlet (bottom). These flow characteristics correspond well with experimental trajectories of particles that are transiently elevated under UV illumination, demonstrating the influence of vertical position on particle routing *via* the local flow field.

The hopping principle can be used to selectively fractionate particles based on interfacial properties. Levitation over high obstacles requires strong phoretic activity, which scales with the effective surface area A_{eff} and determines the *trans*-to-*cis* isomer flux. Under UV illumination (365 nm), porous particles with large A_{eff} levitate higher, whereas plain particles with small A_{eff} show negligible lift. A binary mixture of porous and plain particles thus separates, with porous particles elevated into the higher channel while plain particles remain below (Fig. 6, Video S5). Fluorescein dye in the solution enhances emission from porous particles, providing a visual confirmation of selective levitation during simultaneous UV illumination and emission microscopy.[45,46] The pronounced elevation observed for the porous particles can be attributed to their substantially increased specific surface area compared to that of the plain particle interface. An influence arising solely from differences in intrinsic surface charge between the two particle types can be excluded. As shown in Fig. S4, both silica microparticles exhibit comparable negative zeta potentials in aqueous medium, consistent with the presence of deprotonated surface hydroxyl groups. Upon addition of a cationic surfactant (1 mM), both particle types display a positive zeta potential, which can be ascribed to the adsorption of the surfactant and the formation of a multilayer at the particle interface at the given concentration.[47] Under UV irradiation, the zeta potential remains positive but decreases in magnitude. This reduction is attributed to photoisomerization-induced desorption processes: the predominance of *cis* isomers leads to partial desorption, resulting in a reduced surface coverage by the remaining *trans* isomers in accordance with the *trans*/*cis* population ratio.[46] These observations confirm that the distinct elevation behavior of porous particles is not governed by differences in net surface charge, but rather by their enhanced interfacial area and the associated amplification of interfacial interactions.

Open Access Article. Published on 02 April 2026. Downloaded on 4/25/2026 12:59:56 PM.
This article is licensed under a Creative Commons Attribution 3.0 Unported Licence.

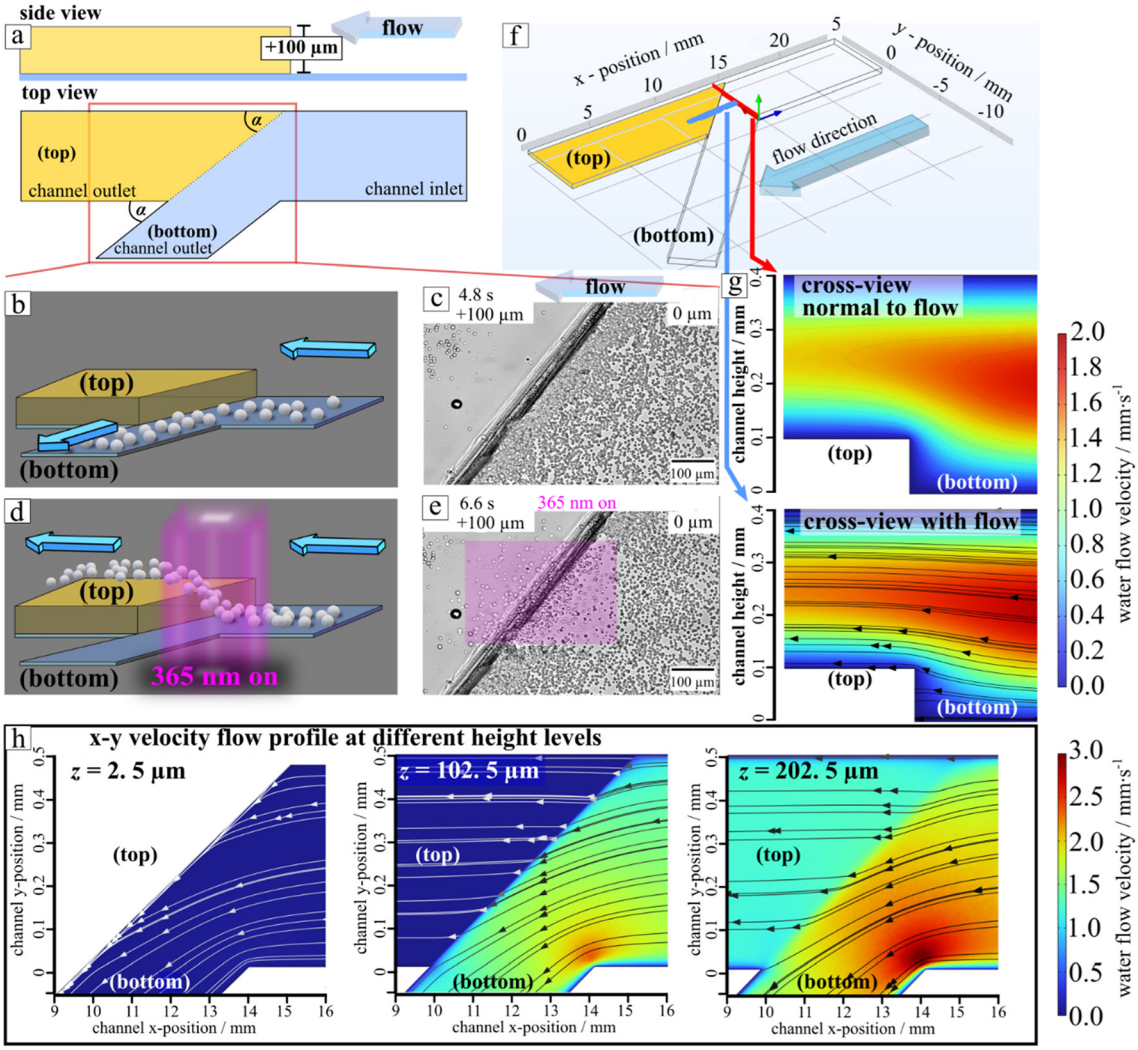

Fig. 5 Conceptual strategy for continuous microparticle separation based on surface properties using light-induced levitation in a laminar flow channel. (a) Schematic of the microfluidic separation device: cross-sectional side view (top) and top view (bottom). (b and c) Under dark conditions, sedimented particles introduced at the channel inlet remain near the bottom and are guided by laminar flow into outlet (bottom). (b) Schematic particle trajectories; (c) optical micrograph from Video S4 at t = 4.6 s (light off) confirming sedimentation-guided flow. (d and e) Upon localized UV illumination (λ = 365 nm), porous particles levitate and are redirected to outlet (top). (d) Micrograph from Video S4 at t = 6.6 s (light on) showing particle levitation; the vertical displacement (~100 µm) is achieved with two layers of transparent tape. (f) COMSOL simulation geometry of the laminar flow field; blue arrow indicates flow direction. Red and blue rectangles mark cross-sectional planes orthogonal and parallel to flow, respectively. (g) Flow field simulations at 150 µL min^{-1} for transverse (y–z, top) and longitudinal (x–z, bottom) planes; color indicates local velocity (mm s^{-1}). (h) Simulated top-view (x–y plane) flow velocities at three vertical positions: 2.5 µm (particle radius), 102.5 µm (channel height + particle radius), and 202.5 µm (above channel). These results illustrate how vertical particle position influences experienced flow, guiding separation behavior.

Furthermore, we note that particle inertia is negligible under the investigated flow conditions. Consequently, the light-induced hopping behavior is interpreted to be governed primarily by advection along the streamlines rather than inertial effects. Based on the theoretical considerations presented in the literature,[36] we calculated a Stokes number (St $\approx 3.32 \times 10^{-4}$) much smaller than 1 for the system as detailed in SI section S8. The obtained result confirms that inertial contributions are minimal and do not significantly influence the particle dynamics.

Furthermore, to quantify the separation efficiency over an operation time of 30 s separation we calculated the number of particles in bright field and emission recording before and after separation. Bright field recording reveals the total number of all particles, porous and plain particles together, so $N_{PSiO_2} + N_{SiO_2}$, while emission recording reveals only the porous particles, N_{PSiO_2}. Thus, one has all important information to calculate the separation efficiency, SE, with respect to porous microparticles equals the fraction of porous particles:

$$SE = \frac{N_{PSiO_2}}{N_{PSiO_2} + N_{SiO_2}} = \frac{N_{emission}}{N_{brightfield}}, \quad (10)$$

similar as used in our previous publications.[27,28] We calculated the separation efficiency before and after the illumination for both channel positions on top of and on the

© 2026 The Author(s). Published by the Royal Society of Chemistry

Open Access Article. Published on 02 April 2026. Downloaded on 4/25/2026 12:59:56 PM.
This article is licensed under a Creative Commons Attribution 3.0 Unported Licence.

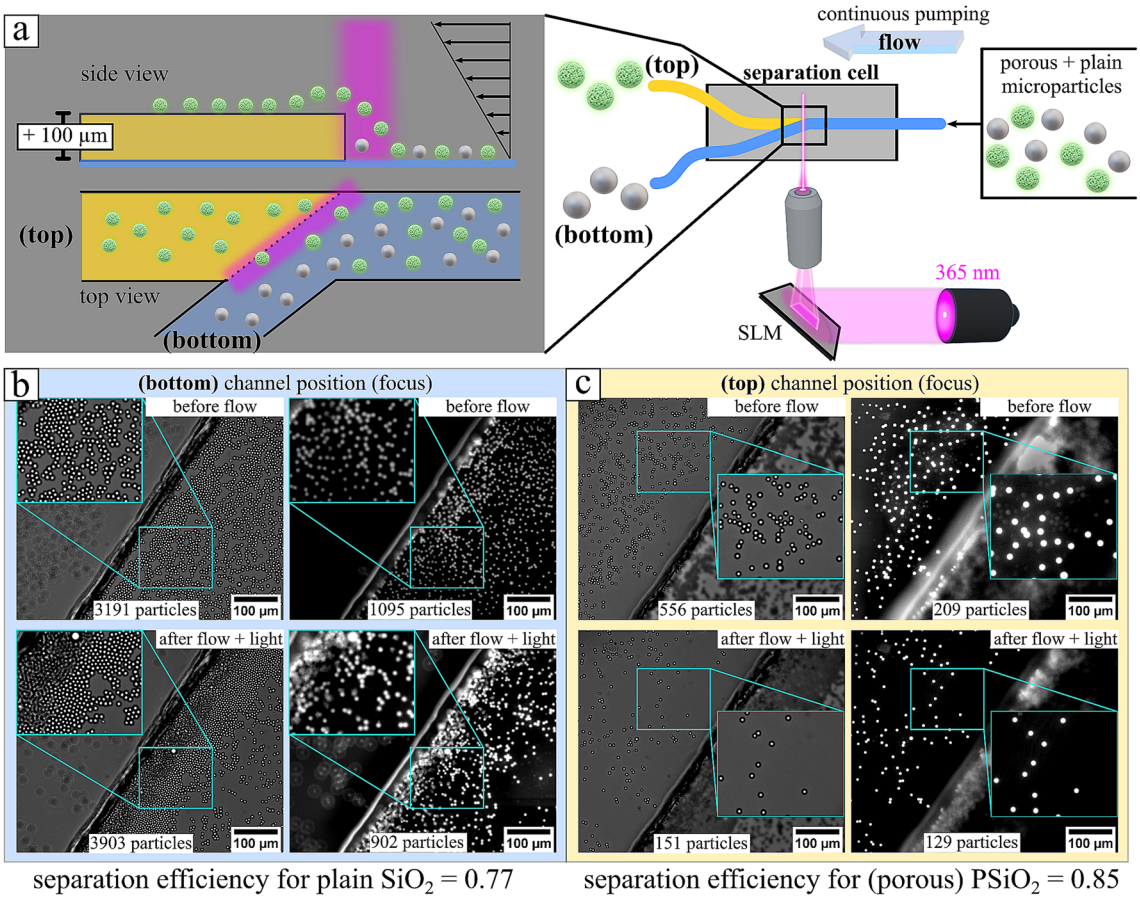

Fig. 6 Experimental demonstration of selective separation of identically sized microparticles based on surface morphology. Microparticles (5 µm) with porous ($PSiO_2$) or plain (SiO_2) surfaces were separated using light-guided levitation in a microfluidic device. (a) Schematic of the separation principle: upon entering the localized UV-illuminated region ("light gate"), porous particles levitate transiently due to enhanced *I*-LDDO, allowing transport *via* laminar flow into the upper outlet (top). Plain SiO_2 particles lack sufficient levitation and remain near the lower surface, exiting *via* outlet I. Statistical or structural variation means not all porous particles cross, but the approach enriches porous particles in outlet II. (b and c) Optical micrographs from Video S5 before and after separation, captured at the bottom (outlet I) and top (outlet II) planes. Each panel shows bright-field and fluorescence (FITC channel) images: porous particles exhibit stronger emission than plain particles, enabling optical differentiation and confirming enrichment in the upper outlet. Details on separation efficiency are provided in SI section S5.

bottom wall labeled in Fig. 6 as bottom or top focus. To demonstrate the change in SE during separation upon UV light illumination we quickly injected the mixture of plain and porous microparticles ($SiO_2/PSiO_2$ = 2/1) to achieve a homogenous distribution of the particles over the entire microfluidic chamber, thus we have initially equal population below and above the wall. Therefore, in the beginning we measured on top (top) a binary fraction of plain and porous particles (Fig. 6c) in a ratio of SE_{PSiO_2} = 0.37 = 209/556, in reasonable agreement with adjusted particle population. After running the demonstration separation upon light activation displayed in Video S5 we observe the porous (bright emitting) microparticles to hop over the wall. Then after the separation, data exhibit in Fig. 6c a dominating fraction of porous particles with a measured SE_{PSiO_2} = 0.85 = 129/151. The efficient enrichment of porous particles in the upper outlet (top) confirms the effectiveness of light-induced levitation and microfluidic separation, as most plain particles remain confined to the lower channel. This performance highlights the selectivity of the method, since only particles with strong phoretic activity linked to their porous surface can overcome the wall barrier under UV illumination and reach outlet II. The separation efficiency (SE) is not perfect, with approximately 15% of plain particles still observed in the upper outlet. Detailed inspection reveals doublets of porous and plain particles (inset, Fig. 6c), where a porous particle can transiently carry a plain particle into the higher channel. Although relatively rare, such particle–particle interactions illustrate the influence of dynamic aggregation on the composition and purity of the separated porous fraction.

Analyzing now the bottom channel (bottom) initially we have a binary mixture of plain and porous particles with a ratio of 0.34 = 1095/3191, in good agreement with value for the initial top channel to be 0.37. After separation we observe a strong accumulation of plain particles, yet porous particles are still present, and it yields according to eqn (10) a SE_{PSiO_2} for porous to be 0.23 = 902/3903. Given the fact that we expect

Open Access Article. Published on 02 April 2026. Downloaded on 4/25/2026 12:59:56 PM.
This article is licensed under a Creative Commons Attribution 3.0 Unported Licence.

at the bottom channel (bottom) an enriched population of plain particles accordingly the value of $SE_{SiO_2} = 1 - SE_{PSiO_2}$ and yields a value of 0.77 demonstrating an accumulation of the plain particle in the same order as for the porous in the upper channel. Quantification in the bottom channel should be approached with caution, as cumulative stacking of multiple particles leads to a significant increase in concentration, making precise particle counting impossible. Although the mixture is clearly not purified, the visible multilayer formation of plain particles indicates that these particles comprise the dominant fraction.

From Video S5 (Fig. 6), we demonstrated selective fractionation of porous particles. Continuous flow allows new particles to be hovered into the upper channel (top) while others are deflected into the lower channel (bottom) by the 40° wall angle. This enables continuous, surface-sensitive separation of particles with strong osmotic/phoretic activity, *i.e.*, those with large surface areas. In this example, porous and plain silica particles of equal size were separated. We emphasize that a direct quantitative relationship between surface area and chemical activity cannot be established due to several additional factors, including surfactant diffusion within pores, surface functionalization, and electrostatic interactions. These factors may either limit or enhance the dynamic exchange of *trans–cis* isomers under illumination, thereby affecting the effective activity (*e.g.*, the measured $U(\lambda)$). This conclusion is drawn from a comparison between surface areas measured *via* nitrogen sorption and surface areas inferred from chemical activity measurements.[35] Nitrogen sorption measurements indicate an approximately fifth-fold larger pore volume for porous particles compared to non-porous particles displayed in Fig. S21 (data taken from reference),[48] whereas an approximately 33-fold stronger chemical activity is reported for the same system in the absence of external flow.[35] This might be attributed that the effective average pore diameter of the porous particles is measured 12 nm, in comparison to non-porous particles to be 2.5 nm (see Fig. S21b), which is in the dimension of the surfactant molecule size to be approximately 2 nm.[49] Thus the strength in chemical activity and the separation potential shown in this work critically depends on the pore size.[47,48] A detailed discussion is provided in the SI (section S6).

Unlike traditional batch-based methods, such as chromatographic or flow-field fractionation,[27,29,30,38] this approach allows continuous operation, enhancing throughput and efficiency. To substantiate this claim, we estimate the mass throughput of fractionated porous particles by quantifying the number of particles crossing the obstacle within the detection area shown in Video S5. Specifically, number of crossing particles were counted within a region of 360 × 410 μm^2 over an observation period of 30 s under continuous illumination.

The calculation in section S9 (SI) and data presented in Fig. S22 indicate that, assuming a homogeneous particle concentration across the channel width w, approximately 1585 particles per second are deflected into the upper channel *via* hydrodynamic levitation. Considering a particle diameter of 5 μm and a material density of 1.8 g cm^{-3}, this corresponds to a processed sample mass of approximately 0.672 mg h^{-1} during one hour of continuous operation. Although the resulting throughput remains within the milligram range, thus being primarily suited for laboratory-scale applications, it exceeds the throughput reported for comparable batch-wise fractionation strategies in the literature[27,29,30,38] by roughly two orders of magnitude.

For comparison, batch-based fractionation typically requires at least 20 min per cycle to achieve complete binary separation under quiescent conditions. In addition to the separation time itself, several preparatory and post-processing steps are required: particle collection after separation, reinjection of a fresh suspension into the separation chamber, careful reconnection of pumping tubes to avoid air bubble formation within tubing and the separation cell, and the re-establishment of fully sedimented initial conditions. These auxiliary procedures generally require an additional preparation time of approximately 10 min. Consequently, a single operational cycle, including separation and preparation, takes about 30 min, allowing for only two cycles per hour of operation. Under these conditions, the achievable sample throughput amounts to approximately 0.004 mg h^{-1}. This comparison clearly demonstrates that the continuous fractionation scheme substantially enhances processing efficiency, increasing the achievable sample throughput by a factor of approximately 160 relatives to conventional batch-based methodologies.[27,29,30,38]

The principle of separation relies on temporarily hovering particles from a lower to a higher wall position *via* microfluidics and illumination of a photoswitchable surfactant at an appropriate wavelength, easily optimized using UV-vis spectroscopy. For continuous separation, it is essential that the injected particles fully sediment onto the bottom substrate before encountering the obstacle. From the injection point to the separation wall, particles are transported along streamlines according to the local flow velocity at their respective vertical positions within the channel.

To provide a simplified estimate of the required sedimentation time and the corresponding horizontal travel distance (*i.e.*, the minimum required injection channel length), we assume that the microparticles are introduced at the top of the rectangular microfluidic channel (*i.e.*, at h). Furthermore, we assume that the sedimentation velocity is not significantly influenced by the perpendicular laminar flow, since it introduces no turbulence in the system. Accordingly, the description of the sedimentation velocity by a low Reynolds number is rectified. Under this assumption, the buoyancy-corrected gravitational force is balanced by the viscous drag force according to Stokes' law, allowing estimation of the terminal sedimentation velocity. Additionally, the particle will follow the streamlines of the laminar flow inside the microfluidic channel during sedimentation. The motion along

© 2026 The Author(s). Published by the Royal Society of Chemistry

Open Access Article. Published on 02 April 2026. Downloaded on 4/25/2026 12:59:56 PM. This article is licensed under a Creative Commons Attribution 3.0 Unported Licence.

the streamlines of the laminar flow is perpendicular to the sedimentation motion. Hence, we can calculate the sedimentation time (t_{sed} = 107.5 s, see section S7 in the SI) independently of motion along the laminar flow, and then calculate the distance traveled along the flow, which is 44 mm. Accordingly, the distance between the injection point and the separation wall should be at least 44 mm or longer (see detailed calculations in the section S7, SI).

Furthermore, precise adjustment of the local illumination position relative to the wall is essential. For accurate positioning of the illumination spot, it is crucial that the particles reach their maximum levitation height at the moment they cross the wall or obstacle. This requirement arises because the levitation process is not instantaneous: particles typically require approximately 3–4 seconds after illumination to reach their fully developed hovering state. Accordingly, the time required for levitation must match the longitudinal travel time of the particles toward the obstacle, such that maximum levitation aligns with the crossing of the obstacle. In our previous study, we mapped the particle velocity field (x–y position) under localized UV illumination on a planar substrate and observed that the maximum levitation height was attained after the particles had traveled a defined distance following UV excitation.[36] Consequently, the illumination spot should be positioned at a corresponding upstream distance on the order of 160 μm before the particles encounter the wall. An increase in flow rate extends the longitudinal distance traveled within the same levitation time under identical illumination conditions. Therefore, with increasing flow rate, the distance between the local light spot and the obstacle must be increased proportionally to ensure that maximum levitation is achieved at the point of crossing.

Additionally, we recommend employing the highest possible light intensity in order to generate the strongest transient levitation enhancement. For strong light-induced chemical activity, as required for the temporal hopping of particles over obstacles, the appropriate choice of surfactant concentration is crucial. The total surfactant concentration should be well above the CMC of the *trans* isomer (CMC_{trans} = 0.5 mM). This ensures that even under illumination, a sufficient fraction of *trans* isomers remains in solution, allowing a rapid dynamic exchange between adsorbing *trans* molecules (with adsorption rate proportional to concentration) and desorbing *cis* molecules.[35] This dynamic exchange sustains a pronounced *cis*-isomer gradient in the vicinity of the particles and thereby maintains strong light-induced chemical activity. Only above a critical *trans*-isomer concentration does the interface remain fully covered with *trans* molecules. At total surfactant concentrations of 2 mM or higher, the interface remains saturated even under UV illumination,[47,50] whereas at lower concentrations significant net desorption at water–glass interfaces has been reported.[50] At the same time, concentrations exceeding 4 mM should be avoided, as this corresponds to the CMC of the *cis* isomer (CMC_{cis} = 4.0 mM). In this regime, the *cis* isomer itself becomes surface-active, which reduces the *cis* concentration gradient and consequently weakens the chemical activity. Therefore, in the experiments presented in this work, the surfactant concentration was set to 1 mM, representing a regime well above CMC_{trans} yet below CMC_{cis}, thereby ensuring robust and reproducible light-induced levitation.

Future improvements include tuning wall height to increase selectivity for less active particles and adjusting wall angles to minimize accumulation of non-hovered particles. Overall, the results demonstrate the feasibility of continuous, surface-sensitive particle separation in microfluidic devices and highlight the potential for further optimization for high-purity, high-throughput applications.

To upscale and generalize the continuous separation principle based on selective light-induced hopping of one particle fraction across others, two boundary conditions are critical: (i) a sufficiently high activity contrast between particle fractions, and (ii) at least one fraction exhibiting intrinsically strong chemical activity. In the following, we qualitatively discuss key engineering parameters governing transferability and scale-up of the separation concept, with particular emphasis on surface/material properties, particle concentration, and the choice of photosensitive surfactant.

Surface and material properties

Light-induced levitation of microparticles has been demonstrated for a broad range of interfacial systems, including porous interfaces,[27,28] chemically functionalized surfaces (hydrophobic and hydrophilic moieties),[27,31] and polymer-modified microparticles.[30] For many of these systems, the *l*-LDDO strength is moderate, resulting in equilibrium levitation heights on the order of 1–2 μm above the bottom substrate. For overcoming macroscopic obstacles (*e.g.*, >100 μm), however, a substantially higher levitation force is required. Since the applied photosurfactant carries a cationic headgroup,[51] preferential adsorption is expected at anionic interfaces,[46] particularly those with high specific surface area. Consequently, negatively charged and porous materials (*e.g.*, silica-based particles[27,28] and activated carbon) are anticipated to exhibit enhanced interfacial surfactant accumulation and thus stronger *l*-LDDO activity. Similarly, microgels and highly hydrated polymer networks, especially those incorporating anionic functional groups can generate pronounced chemical gradients under illumination.[34,52] From a separation engineering perspective, these material classes provide a larger activity contrast window and are therefore particularly suitable for selective fractionation based on light-triggered hopping over obstacles.

Particle concentration effects

The hopping mechanism is comparatively robust over several orders of magnitude in particle concentration.[36] However, experimental observations indicate that levitation height decreases with increasing particle number density.[36] This behavior can be attributed to collective effects such as local

Open Access Article. Published on 02 April 2026. Downloaded on 4/25/2026 12:59:56 PM. This article is licensed under a Creative Commons Attribution 3.0 Unported Licence.

depletion of product gradients. As a result, the effective activity contrast between fractions reduces with increasing concentration, rendering selective separation progressively more challenging. The extent of this limitation depends on the natural light induced activity strength of the respective particle fractions. For scale-up considerations, concentration-dependent transport phenomena therefore represent a key parameter.

Photosensitive surfactant selection

The choice of photosensitive surfactant constitutes a central control parameter in the separation process. In the present study, an azobenzene-based cationic surfactant was employed, for which photoisomerization kinetics in bulk[33] and at interfaces,[35,50] as well as adsorption/desorption dynamics at solid–liquid interfaces (with[50] and without illumination[47]), have been extensively characterized in the literature. Reported kinetic data indicate that the relative rates of adsorption/desorption and photoisomerization enable a sustained dynamic exchange between *trans*- and *cis*-isomers under continuous illumination. This dynamic steady state generates sufficiently strong and spatially confined chemical gradients at solid–liquid-interfaces to induce active levitation of microparticles in aqueous media. Importantly, the propulsion strength and equilibrium position can be precisely modulated *via* illumination wavelength[28] and intensity,[35] providing a high degree of external process control.

Variations in hydrophobic chain length and headgroup architecture of the surfactant molecule significantly affect interfacial packing density,[53] adsorption equilibria, and desorption kinetics of both isomers, and therefore directly modulate the magnitude of the light-induced chemical activity. While LDDO has been reported for surfactants with different alkyl chain lengths, the strongest effects to date have been observed for the compound presented in Scheme 1. Current literature suggests that cationic headgroups with minimal steric demand promote higher interfacial accumulation compared to bulkier analogues,[52,53] thereby enhancing gradient formation.

Nevertheless, the selection of an optimal photosensitive surfactant is inherently application-specific and multidimensional, involving trade-offs between molecular volume change upon isomerization, photostability, quantum yield, adsorption strength, and dynamic exchange potential.[53] Among available photoresponsive systems,[54–58] azobenzene derivatives remain particularly attractive due to their pronounced conformational change during isomerization and low photodegradation, albeit at moderate quantum yield.[59] The latter can be compensated by applying high photon flux (*i.e.*, increased illumination intensity), enabling high conversion rates and sustained gradient formation.[27,28] For a comprehensive discussion on material-specific classification of light-induced chemical activity and surfactant selection strategies, the reader is referred to the corresponding perspective article published elsewhere.[53]

Conclusion

We demonstrated that with the combination of a photoactive surfactant and microfluidics one can separate equally sized microparticles by their differences in their interface, where the principle of separation could run continuously.

The principle works by hovering sedimented particles over obstacles/walls much bigger than the size of the particles. To that end particles are induced osmotically/phoretically active, which produces, leads to selective levitation of only strongly active particles. Then, simultaneously, an external fluid flow carries the particles in an upper channel position. Now particles with difference in surface properties likewise porous *versus* plain particle are hovering differently high and by so, only the porous (~strong active) can be guided into the higher channel. The plain particles remain effectively non-hovered and are deflected from the wall, where the flow guides them into the lower channel. Such strong levitation requires locally collimated light through the microscope objective, which not only focuses on the applied light intensity but also needs a special wavelength of illumination. Both parameters must increase the initial burst (~initial photoisomerization kinetics) of adsorbed *trans*-isomers by that porous particles are temporary so strong active to pass by a wall lift height of 100 um. For azobenzene containing surfactants such strong activities could be achieved with UV light (365 nm).

To predict the wavelength needed for high levitation (~strong activity) of the particles, this can be estimated from the extinction coefficient of the photo switch, a strait forward value quickly to be obtained from UV-vis spectroscopy. The physical principles result from the photoisomerization rate constant, which is proportional to the extinction coefficient.

Materials and methods

Microfluidic chambers and microparticles

Microfluidic experiments were conducted using commercially available flow chambers (μ-Slide^{VI}, Ibidi GmbH), featuring a glass-bottom coverslip suitable for high-resolution optical microscopy. Each chamber has a void volume of 40 μL.

Two types of silica-based colloidal particles were employed in the study: commercial porous silica microparticles with mean diameters of (3 ± 1) μm and (5 ± 1) μm, otherwise unmodified, were obtained from micromod GmbH (sicastar® 43-00-503). These particles possess internal porosity. Non-porous (plain) silica colloids with narrowly distributed diameters of (4 ± 0.1) μm and (5 ± 0.1) μm otherwise unmodified, were sourced from microparticles GmbH (SiO_2-F-SC260-2).

Azobenzene containing surfactant

The azobenzene-containing surfactant, **C_4-Azo-OC_6TMAB** (azobenzene-functionalized trimethylammonium bromide), was synthesized in accordance with previously reported methodologies. Structurally (Scheme 1), the molecule consists of a cationic trimethylammonium bromide

© 2026 The Author(s). Published by the Royal Society of Chemistry

Open Access Article. Published on 02 April 2026. Downloaded on 4/25/2026 12:59:56 PM. This article is licensed under a Creative Commons Attribution 3.0 Unported Licence.

headgroup connected to an azobenzene core *via* a hexamethylene spacer. The azobenzene unit is further functionalized with a terminal butyl chain, enhancing its amphiphilic character.

A stock solution of the surfactant was prepared at a concentration of 10 mM in ultrapure water (Milli-Q, resistivity $>$ 18 MΩ cm) and subsequently diluted to 1 mM for experimental applications involving microparticle dispersions.

The photophysical behavior of the surfactant was characterized *via* UV-visible absorption spectroscopy. In its thermodynamically stable *trans*-configuration, the molecule exhibits a π–π* transition centered at 351 nm. Upon photoisomerization to the *cis*-isomer, the absorption profile changes markedly, showing a blue-shifted π–π* transition at 313 nm and the emergence of an n–π* transition at 437 nm. The *cis*-isomer is metastable and undergoes thermal relaxation back to the *trans*-form with a half-life of approximately 48 hours under ambient dark conditions or under continuous red-light irradiation (λ = 625 nm) at 23 °C.[33]

Sample preparation

Aqueous colloidal dispersions are mixed with a stock solution of photosensitive surfactants to reach a final surfactant concentration of 1 mM. The mixtures are equilibrated for a minimum of 24 hours prior to any measurements to ensure homogeneous distribution and equilibration of the surfactant within the dispersion. For measurements, the surfactant–colloid mixture is introduced into the microfluidic chamber, where gravitational sedimentation leads to the accumulation of particles on the bottom glass surface. The chamber is connected to a syringe pump (PhD Ultra, Harvard Apparatus), enabling controlled fluid manipulation. The entire fluidic system including the chamber, syringe, and connecting tubing is prefilled with the same aqueous solution containing 1 mM of the photosensitive surfactant to maintain chemical consistency throughout the setup. All samples are handled and stored under red light or in the dark to prevent unintended photoisomerization of the azobenzene-containing surfactant. Measurements are carried out at ambient conditions, with the temperature maintained at T = 23 ± 1 °C.

Sample preparation with fluorescein dye

Fluoresceine was used as the fluorescent probe for all emission imaging experiments. Prior to mixing with particle mixture of porous ($PSiO_2$) and plain (SiO_2) particles (D = 5 μm, $c_{particles,total}$ = 0.3 mg mL^{-1}, ratio $SiO_2/PSiO_2$ = 2/1), the surfactant solution (c = 1 mM) is mixed with fluorescein (c = 15 μM). Similar as above, the entire fluidic system including the chamber, syringe, and connecting tubing contain the surfactant-dye solution. Details of measurement conditions are shown in SI (section S5).

Preparation of modified glass substrate for microfluidic integration

A standard borosilicate microscope glass slide (commercially available) was modified to create a patterned surface suitable for microfluidic chamber. Two parallel layers of transparent pressure-sensitive adhesive tape (Tesa GmbH) were applied to the substrate surface. These tape layers were aligned and trimmed such that the resulting boundary edges formed an angle of ~40° relative to the anticipated fluid flow direction within the final microfluidic chamber. Selective regions of the adhesive tape, corresponding to the future microchannel area, were carefully scraped using a precision utility blade under light pressure to avoid damaging the underlying glass. This defined the channel bottom substrate of the microfluidic channel. Following the tape removal, residual adhesive in the exposed regions was immediately cleaned using a minimal volume of high-purity methanol. The cleaning was performed with care to minimize solvent interaction with the remaining adhered tape sections, preserving their integrity. The substrate was then left to dry under ambient conditions until complete methanol evaporation was confirmed.

Subsequently, the cleaned and patterned glass substrate was aligned and bonded to a commercial microfluidic channel (sticky-Slide VI$^{0.4}$, Ibidi GmbH), which incorporates a pre-defined chamber geometry. The microfluidic channel dimensions are approximately: length L = 17 mm, width w = 3.8 mm, and height h = 0.54 mm corresponding to a void volume of approximately 40 μL.

Zeta potential measurements

Zeta potential is calculated from the electrophoretic mobility measured using commercial zetasizer (Nano-ZS, Malvern Instruments, Ltd., Malvern, UK). Microparticles (c_{mass} = 0.1 mg ml^{-1}) are dispersed in MilliQ or aqueous solution containing the azobenzene surfactant solution (c = 1 mM). Prior to measurements dispersion are sonicated and immediately injected into the measurement cell, an directly measured. Data containing UV illumination is exposed for 12 min under irradiation with UV light (365 nm, I = 10 mW cm^{-2}), followed by sonication for 10 s.

Nitrogen sorption analysis

The porous and non-porous commercial stock colloidal suspension was purified by two successive washes with Millipore-grade water to eliminate residual contaminants. The cleaned suspensions were subsequently freeze-dried overnight under high vacuum (<1 mbar) using a Schlenk line. The resulting dry powders and approximately 100 mg were used for N_2 sorption.

Nitrogen sorption measurements

Prior to analysis, the dried samples were accurately weighed, transferred into analysis cells, and degassed under vacuum at

Open Access Article. Published on 02 April 2026. Downloaded on 4/25/2026 12:59:56 PM.
This article is licensed under a Creative Commons Attribution 3.0 Unported Licence.

300 °C for 3 h using a BELPREP VAC III preparation system (Microtrac). Nitrogen adsorption–desorption isotherms were recorded with a BELSORP MAX surface area and porosity analyzer (Microtrac). Depending on the porosity of the samples, measurement times ranged from 18 h (porous particles) to 43 h (non-porous particles). Adsorption data are presented as the adsorbed nitrogen volume plotted against the corresponding relative pressure.

COMSOL simulations. COMSOL Multiphysics 6.3 (COMSOL Inc., Burlington, MA) was used to simulate fluid flow. The model was implemented in 3D using a finer, physics-controlled mesh consisting of 4 974 542 domain elements, 286 916 boundary elements, and 6669 edge elements. (Fig. S6). Flow within the system was modeled under steady-state laminar conditions with a fixed volumetric flow rate of 150 μL min^{-1}, since Reynolds number under study is low, Re ~100. A no-slip boundary condition was applied to all walls.

Image acquisition and light source. An inverted optical microscope (Olympus IX73) equipped with dual-wavelength illumination capabilities was employed for sample observation and photoactivation. The illumination system enabled both global and localized exposure of the sample to two distinct wavelengths: 625 nm (red) and a secondary wavelength denoted as *X* nm.

The 625 nm wavelength served as image acquisition tool, as it does not induce photo-isomerization of the photosensitive surfactant. In contrast, the secondary wavelength (*X* nm) was selected based on its ability to induce photo-isomerization. The LED illumination system was configured to enable both global and localized collimation. For global illumination, the light was collimated through the ocular pathway, resulting in uniform exposure across the entire sample area. For localized illumination, the light beam was first shaped using a spatial light modulator (SLM), enabling precise spatial control of the illumination pattern. The modulated beam was then directed through the objective lens to selectively illuminate defined regions of the sample at the focal plane.

This dual-mode collimation approach allowed flexible photoactivation strategies, facilitating both homogeneous and spatially resolved control of light-responsive surfactants. A detailed schematic of the optical setup and beam collimation pathways is provided in Fig. S23 (SI, microscope setup).

After transmission through the sample, all wavelengths below 625 nm were effectively blocked using a 580 nm long-pass optical filter (Thorlabs GmbH), thereby ensuring that only the red light (625 nm) reached the detection system. This optical filtering enabled selective imaging under non-photoactivating conditions, minimizing interference from photoresponsive wavelengths during video acquisition. All LED light sources used in the study were obtained from Thorlabs GmbH, with the following center wavelengths and model numbers: 365 nm (M365LP1), 375 nm (M375L4), 385 nm (M385L3), 395 nm (M395L5), 405 nm (M405L4-C1), 415 nm (M415L4), 430 nm (M430L5), 455 nm (M455L4), 490 nm (M490L4), 505 nm (M505L4-C1), 530 nm (M530L4), and 625 nm (M625L4). Video recordings were performed using a Hamamatsu ORCA-Flash camera at a frame rate of 30 frames per second, capturing dynamics exclusively under red-light illumination.

Fluorescence imaging. Fluorescence imaging was performed using the inverted microscope equipped with standard FITC filter sets (excitation: 488 nm; emission: 500–550 nm). Fluoresceine fluorescence was excited using the white light source Xe–Hg light source, where low band pass filter was used for spectral excitation range 350–490 nm. This allows a simultaneous illumination of UV light for photoisomerization of the surfactant to hop up the particles and the excitation of the dye. Emission was collected using a 505–530 nm high bandpass filter. Images were acquired using a objective with 20× magnification/0.4 NA and are processed using the software package Fiji/Image. Imaging parameters such as light source power, gain, and exposure time (0.5 s) were held constant between experimental conditions to enable bright emissions of porous and a weak emission of non-porous particles.

Kinetic investigations. Photoisomerization rate constants were analyzed and published on our previous publication.[28,33] Briefly: UV-vis kinetics were recorded using a Cary 5000 UV-vis spectrophotometer (Agilent Technologies, USA) by using its kinetics module. A quartz cuvette (Hellma Analytics) with 1 cm spacing was filled with 1.8 mL of the aqueous sample and sealed to maintain constant concentration. The entire sample volume was uniformly irradiated with an LED at wavelength λ, and absorbance at 376 nm was monitored, normalized to its initial value, and fitted to the following exponential isomerization model:

$$\frac{\mathrm{Abs}_{376}(t)}{\mathrm{Abs}_{376,0}} = \frac{c(t)}{c_0} = \frac{k_{CT} + k_{TC}\cdot\exp(-[k_{TC} + k_{CT}]\cdot I\cdot t)}{k_{TC} + k_{CT}} = \frac{k_{CT} + k_{TC}\cdot\exp\left(-\frac{t}{\tau}\right)}{k_{TC} + k_{CT}} \quad (11)$$

here, t is the time, I is the light intensity, k_{TC} and k_{CT} are the *trans* → *cis* and *cis* → *trans* photo-isomerization rate constants, respectively, and $\tau = 1/[(k_{TC} + k_{CT})\cdot I]$.

This allows calculation of k_{TC} given by:

$$k_{TC} = \frac{1}{\tau\cdot I} - \frac{c_{eq}}{c_0}\cdot\frac{1}{\tau\cdot I}. \quad (12)$$

Light intensity at the sample location was measured prior to each experiment using a Thorlabs S170C power meter and set to 1 mW cm^{-2} for UV-vis studies (and 11.5 mW for microscopy). Detailed derivations, interpretation and model description are published elsewhere.[28]

Volumetric flow rate to shear rate. The shear rate S for a rectangular channel geometry with channel dimensions: length l = 17 mm, height h = 0.54 μm and width w = 3.8 mm (experimental conditions in this work) is calculated by the expression:[60]

© 2026 The Author(s). Published by the Royal Society of Chemistry

Open Access Article. Published on 02 April 2026. Downloaded on 4/25/2026 12:59:56 PM.
This article is licensed under a Creative Commons Attribution 3.0 Unported Licence.

$$S = \frac{Q}{2 \cdot h^2 \cdot w}\left[\frac{1}{12} - \frac{16}{\pi^5}\frac{h}{w}\right]^{-1}, \quad (13)$$

where Q is the adjusted volumetric flow rate equal to 150 μL min^{-1} always, which correspond to a shear rate S = 14.98 s^{-1}.

Video tracking

Motion videos were acquired using an inverted Olympus microscope (IX73) equipped with a Hamamatsu ORCA-Flash 4.0 scientific CMOS camera or Olympus MFD 2 – IX53, 73.

Depending on the configuration, frame rates were set to 30 fps (ORCA-Flash 4.0) or 15 fps (MFD2-controlled IX53/IX73).

Image acquisition was conducted under red illumination (I = 0.5 mW cm^{-2}) to minimize photochemical disturbances. For illumination, a collimated LED at wavelength λ was directed either from above over the condenser (global illumination) or from below over the objective (illumination) depending on experimental requirements. Prior to each recording session, the aqueous surfactant solution (c = 1 mM) with pre-dispersed microparticles was irradiated at λ for 1 minute at a power of 11.5 mW to ensure attainment of photo-stationary state and equilibrium isomer population. Motion recording was performed by previously sedimented all microparticles onto the bottom glass interface of the rectangular microfluidic channel with 17 mm channel length, 3.8 mm channel depth and 0.54 mm channel height (μ-slide^{VI} with a glass bottom cover slip (Ibidi GmbH)).

A typical 45-second motion-recording sequence captures microparticle trajectories along flow streamlines with the following precisely defined illumination protocol:

1. Initial phase (0–5 s)

A 5-second period without irradiation, allowing observation of baseline particle motion under passive flow conditions.

2. Irradiation phase (5–25 s)

A 20-second interval of illumination at wavelength X (I = 11.5 mW cm^{-2}), activating photoresponsivity behavior while continuously recording particle dynamics.

3. Post-illumination phase (25–45 s)

A final 25-second interval without irradiation, capturing relaxation or persistent effects in the absence of light.

This structured timing ensures a controlled analysis of both the immediate and lasting photo driven responses of the microparticles within the flow system. Each measurement was performed under applied constant pressure driven flow using a syringe pump (Ph.D. ultra, Harvard apparatus) with a flow rate of 150 μL min^{-1}.

Motion analysis of particles. Image analysis was performed by converting grayscale video frames into binary images *via* a thresholding procedure, wherein background pixels were assigned to a value of zero (black) and particle pixels a value of one (white). Particle tracking was achieved by determining the displacement of the center of mass of each identified particle between two frames. At each time step, the momentum particle velocity was computed for each particle and averaged over all particles present within the field of view. These mean velocities were recorded as a function of time, with the corresponding standard deviation representing the frame-wise variability among particles. For analyses involving summarized time-average quantities, only data collected after the system achieved a steady-state velocity were included. Steady-state was operationally defined as the period commencing 15 seconds after the onset of continuous illumination. We used a python software with several software packages: Bokeh, Numpy, OpenCV-python, Matplotlib, Openpyxl, Pandas, SciPy.[27,28,31]

Statistical analysis. Statistical analysis is done similar to our previous publication[27,28,31] with same set of software Python software package. We calculated the time resolved average velocity U from the sample size n (number of particles) of individual velocity U_i for each frame-to-frame and we averaged using the arithmetic mean to obtain:

$$\bar{U} = \frac{1}{n}\left(\sum_{i=1}^{n} U_i\right) \quad (14)$$

and the corresponding standard deviation, denoted by σ, computed as the square root of the unbiased sample variance using a denominator of $n - 1$, where n is the sample size:

$$\sigma = \sqrt{\frac{1}{n-1}\sum_{n=i}(U_i - \bar{U})^2}. \quad (15)$$

All data is treated without evaluation of outliers.

Author contributions

M. B. designed and supervised the project and wrote the manuscript. F. R., D. V. M. performed experiments, analysis, and wrote manuscript together with S. S. C. B., I. M., S. L. and A. S. performed experiments and analysis. N. L. synthesized the photosensitive surfactant. Y. G. performed COMSOL simulations. All the authors were involved in the preparation of the manuscript. All the authors have read and approved the final manuscript.

Conflicts of interest

The authors declare no competing financial interests.

Data availability

The data supporting this article have been included as part of the SI.

Primary data (uploaded Video files) supporting this article have been included as part of the supplementary information (SI) uploaded on publisher website.

Supplementary information is available. See DOI: https://doi.org/10.1039/d5lf00341e.

Open Access Article. Published on 02 April 2026. Downloaded on 4/25/2026 12:59:56 PM. This article is licensed under a Creative Commons Attribution 3.0 Unported Licence.

Acknowledgements

M. B. acknowledges financial support by the National German Science Foundation (DFG) through the grant BE 7745/1-1. A. T. and A. N. acknowledge funding from the University of Potsdam (grant 5317000).

References

1 X. Yang, F. Yu, H. Shang, Z. Li, S. Wang, Y. Xing and X. Gui, *Powder Technol.*, 2025, **453**, 120594.
2 Y. Deng, Y. Cai, Z. Sun, J. Lia, C. Liu, J. Weng, W. Li, C. Liu, Y. Wang and D. Zhao, *J. Am. Chem. Soc.*, 2010, **132**(24), 8466.
3 M. A. M. Gijs, F. Lacharme and U. Lehmann, *Chem. Rev.*, 2010, **110**, 1518.
4 Y. Ding, Y. Yan, H. Wang, X. Wang, T. Hu, S. Tao and G. Li, *ACS Appl. Mater. Interfaces*, 2018, **10**, 48.
5 H. Kim, B. Han, J. Choo and J. Cho, *Angew. Chem., Int. Ed.*, 2008, **47**, 10151–10154.
6 H. Liu, X. Liu, W. Li, X. Guo, Y. Wang, G. Wang and D. Zhao, *Adv. Energy Mater.*, 2017, **7**, 1700283.
7 A. Bielefeld, D. A. Weber and J. Janek, *J. Phys. Chem. C*, 2018, **123**, 1626–1634.
8 Y. Wang, M. Zhang, Y. Lai and L. Chi, *Nano Today*, 2018, **22**, 36–61.
9 Y. Kim, X. Dong, S. Chae, G. Asghar, S. Choi, B. Jun Kim, J.-Y. Choi and H. K. Yu, *Adv. Mater.*, 2022, **35**, 2204775.
10 R. Ahmed, I. Block, F. Otte, C. Günter, A. Duarte-Rodrigues, P. Hesemann, A. Banerji and A. Taubert, *Chemistry*, 2023, **5**, 1124–1137.
11 S. Wong, N. Ngadi, I. M. Inuwa and O. Hassan, *J. Cleaner Prod.*, 2018, **175**, 361–375.
12 I. Block, H. M. Rawel, T. Klamroth, C. Günter, J. Kim, F. Loepthien, S. K. Gahlaut, I. Bald and A. Taubert, *ACS Omega*, 2025, **10**, 4614–4623.
13 D. G. Ghosh Dastidar, S. Saha and M. Chowdhury, *Int. J. Pharm.*, 2018, **548**, 34–48.
14 S. Pöttgen, M. Mazurek-Budzyńska and C. Wischke, *Int. J. Pharm.*, 2025, **672**, 125340.
15 L. Wu, S. Bai and Y. Sun, *Biotechnol. Prog.*, 2008, **19**, 1300–1306.
16 K. J. Stine, *Adv. Carbohydr. Chem. Biochem.*, 2017, **74**, 61–136.
17 P. Bayat and P. Rezai, *Soft Matter*, 2018, **14**, 5356.
18 J. Oakey, J. Allely and D. W. M. Marr, *Biotechnol. Prog.*, 2002, **18**(6), 1439.
19 M. Yamada, M. Nakashima and M. Seki, *Anal. Chem.*, 2004, **76**(18), 5465.
20 J. F. Ashley, C. N. Bowman and R. H. Davis, *AIChE J.*, 2013, **59**(9), 3444.
21 G. Brans, A. Van Dinther, B. Odum, C. G. P. H. Schroën and R. M. Boom, *J. Membr. Sci.*, 2007, **290**(1–2), 230.
22 M. Iranmanesh and J. Hulliger, *Chem. Soc. Rev.*, 2017, **46**, 5925.
23 A. Dalili, E. Samiei and M. Hoorfar, *Analyst*, 2019, **144**, 87.
24 C. Sophonsiri and E. Morgenroth, *Chemosphere*, 2004, **55**(5), 691.
25 A. Chakra, C. Puijk, G. T. Vladisavljević, C. Cottin-Bizonne, C. Pirat and G. Bolognesi, *J. Colloid Interface Sci.*, 2025, **693**, 137577.
26 J. Zheng, J. Chen, Y. Jin, Y. Wen, Y. Mu, C. Wu, Y. Wang, P. Tong, Z. Li, X. Hou and J. Tang, *Nature*, 2023, **617**, 499–506.
27 M. Bekir, M. Sperling, D. Vasquez-Muñoz, C. Braksch, A. Böker, N. Lomadze, M. N. Popescu and S. Santer, *Adv. Mater.*, 2023, **35**, 2300358.
28 D. Vasquez Muñoz, F. Rohne, I. Meier, A. Sharma, N. Lomadze, S. Santer and M. Bekir, *Small*, 2024, **20**, 202403546.
29 V. Muraveva, M. Bekir, N. Lomadze, R. Großmann, C. Beta and S. Santer, Interplay of diffusio- and thermo-osmotic flows generated by single light stimulus, *Appl. Phys. Lett.*, 2022, **120**, 231905.
30 A. Sharma, F. Rohne, D. Vasquez-Muñoz, S.-H. Jung, N. Lomadze, A. Pich, S. Santer and M. Bekir, *Small Methods*, 2024, **8**, 202400226.
31 D. Vasquez Munoz, F. Rohne, I. Meier, C. Braksch, N. Lomadze, A. Heraji Esfahani, A. Nitschke, A. Taubert, S. Santer, M. Hartlieb and M. Bekir, *Small Sci.*, 2024, **4**, 2400146.
32 D. Vasquez-Muñoz, M. Nicola Popescu, A. Sharma, F. Rohne, I. Meier, P. Ortner, S. Loebner, J. R. Benson, N. Lomadze, S. Eickelmann, S. Santer and M. Bekir, *Small*, 2025, **21**, 2500012.
33 P. Arya, J. Jelken, N. Lomadze, S. Santer and M. Bekir, *J. Chem. Phys.*, 2020, **152**, 024904.
34 A. Sharma, M. Bekir, N. Lomadze and S. Santer, *Molecules*, 2021, **26**, 19.
35 M. Bekir, A. Sharma, M. Umlandt, N. Lomadze and S. Santer, *Adv. Mater. Interfaces*, 2022, **9**, 2102395.
36 F. Rohne, D. Vasquez-Muñoz, S. Santer and M. Bekir, *J. Chromatogr. A*, 2025, **1762**, 466368.
37 J. Happel and H. Brenner, *Low Reynolds Number Hydrodynamics*, Prentice-Hall, Englewood Cliffs, NJ, 1965.
38 H. Brenner, The slow motion of a sphere through a viscous fluid towards a plane surface, *Chem. Eng. Sci.*, 1961, **16**, 242–251.
39 F. Rohne, D. Vasquez Muñoz, I. Meier, N. Lomadze, S. Santer and M. Bekir, *Lab Chip*, 2025, **25**, 4106–4118.
40 E. Titov, A. Sharma, N. Lomadze, P. Saalfrank, S. Santer and M. Bekir, *ChemPhotoChem*, 2021, **5**, 926.
41 P. S. Williams, M. H. Moon, Y. Xu and J. C. Giddings, *Chem. Eng. Sci.*, 1996, **51**, 4477–4488.
42 P. S. Williams, T. Koch and J. C. Giddings, *Chem. Eng. Commun.*, 1991, **111**, 121–147.
43 P. S. Williams, L. Seungho and J. C. Giddings, *Chem. Eng. Commun.*, 1994, **130**, 143–166.
44 I. S. Woo, E. C. Jung and S. Lee, *Talanta*, 2015, **132**, 945–953.
45 A. K. Mathur, C. Agarwal, B. S. Pangtey, A. Singh and B. N. Guptam, *Int. J. Cosmet. Sci.*, 1988, **10**, 213–218.
46 J. K. Salem, I. M. El-Nahhal and S. F. Salama, *Chem. Phys. Lett.*, 2019, **730**, 445–450.
47 M. Umlandt, D. Feldmann, E. Schneck, S. Santer and M. Bekir, Adsorption of Photoresponsive Surfactants at Solid –Liquid Interface, *Langmuir*, 2020, **36**, 14009.

© 2026 The Author(s). Published by the Royal Society of Chemistry

Open Access Article. Published on 02 April 2026. Downloaded on 4/25/2026 12:59:56 PM.
This article is licensed under a Creative Commons Attribution 3.0 Unported Licence.

48 F. Rohne, D. Vasquez Muñoz, I. Meier, A. Nitschke, F. Schmitt, N. Lomadze, M. Reifarth, A. Taubert, S. Santer and M. Bekir, Particle-Based Detection of Surface Chemistry via Optical Microscopy—Integrating Microfluidics, Light-Induced Activity of Colloids and Data Science, *Small Methods*, 2026, **10**, e02329.
49 M. Montagna and O. Guskova, Photosensitive Cationic Azobenzene Surfactants: Thermodynamics of Hydration and the Complex Formation With Poly(methacrylic acid), *Langmuir*, 2018, **34**, 311–321.
50 M. Umlandt, P. Ortner, N. Lomadze, M. Bekir, S. Santer and Y. D. Gordievskaya, *Langmuir*, 2025, **41**, 29567–29577.
51 S. Santer, *J. Phys. D: Appl. Phys.*, 2017, **51**, 013002.
52 M. Bekir, S. Loebner, A. Kobyshev, N. Lomadze and S. Santer, Photosensitive Spherical Polymer Brushes: Light Triggered Process of Particle Repulsion, *Processes*, 2023, **11**, 773.
53 M. Bekir, J. Gurke and M. Reifarth, *ChemSystemsChem*, 2024, 202400026.
54 M. Schnurbus, R. A. Campbell, J. Droste, C. Honnigfort, D. Glikman, P. Gutfreund, M. R. Hansen and B. Braunschweig, *J. Phys. Chem. B*, 2020, **124**, 6913.
55 C. Honnigfort, L. Topp, N. García Rey, A. Heuer and B. Braunschweig, *J. Am. Chem. Soc.*, 2022, **144**, 4026.
56 M. Reifarth, M. Bekir, A. M. Bapolisi, E. Titov, F. Nußhardt, J. Nowaczyk, D. Grigoriev, A. Sharma, P. Saalfrank, S. Santer, M. Hartlieb and A. Böker, *Angew. Chem., Int. Ed.*, 2022, **61**, e202114687.
57 R. Klajn, *Chem. Soc. Rev.*, 2014, **43**, 148.
58 D. H. Waldeck, Photoisomerization Dynamics of Stilbenes, *Chem. Rev.*, 1991, **91**, 415–436.
59 L. W. Giles, C. F. J. Faul and R. F. Tabor, *Mater. Adv.*, 2021, **2**, 4152.
60 M. J. Boussinesq, *J. Math. Pures Appl.*, 1868, **13**, 377–424.